

PAPER • OPEN ACCESS

Validation of numerical models for flow simulation and wave propagation along human aorta

To cite this article: N Kizilova and J Mizerski 2018 *J. Phys.: Conf. Ser.* **1101** 012014

View the [article online](#) for updates and enhancements.

You may also like

- [Population-based reference values for 4D flow MRI derived aortic blood flow parameters](#)
Marie Schafstedde, Lina Jarmatz, Jan Brüning et al.
- [Automatic thoracic aorta calcium quantification using deep learning in non-contrast ECG-gated CT images](#)
Federico N Guilenea, Mariano E Casciaro, Gilles Soulat et al.
- [Use of human aortic extracellular matrix as a scaffold for construction of a patient-specific tissue engineered vascular patch](#)
Li-Ping Gao, Ming-Jun Du, Jing-Jing Lv et al.

ECS
The
Electrochemical
Society
Advancing solid state &
electrochemical science & technology

DISCOVER
how sustainability
intersects with
electrochemistry & solid
state science research

Validation of numerical models for flow simulation and wave propagation along human aorta

N Kizilova¹ and J Mizerski²

¹Institute of Aeronautics and Applied Mechanics, Warsaw University of Technology, Warsaw, Poland

²Interdisciplinary Centre for Mathematical and Computational Modelling, Warsaw University, Warsaw, Poland

E-mail: n.kizilova@gmail.com

Abstract: Numerical computations on 2d model of blood flow along human aorta based on incompressible axisymmetric Navier-Stokes equations for blood and momentum equations for incompressible viscoelastic arterial wall are compared to the blood flow oscillation curves measured in vivo by Doppler ultrasound in the larger systemic arteries of healthy volunteers. The analysis of the wave propagation and reflection along the geometrical 91-tube model of aorta as a tube with side branches is based on Lighthill's theory of waves in arteries. It is shown due to individual geometry positive wave reflections at some aortic branches and aortic bifurcation may lead to increase of the pressure amplitudes, high pressure and wall shear stress oscillations that may lead to wall damage and development of aortic aneurism and stenoses of branched arteries. The numerical results obtained on the linearized 2d and nonlinear 1d models are compared to the in vivo pressure and flow measurements along the aorta and in its branches. A good qualitative correspondence is obtained. The model can be used for determination of the individual parameters for patient-specific cardiovascular models.

1. Introduction

Mathematical modeling of blood flow and pulse wave (PW) propagation in arterial vasculatures and novel methods of analysis of the pressure $p(t)$ and flow $v(t)$ waveforms have become important constituents of contemporary medical diagnostics of the cardiovascular diseases [1]. Such approaches related to the computational medicine based on the vast detailed numerical computations on individual patient specific mathematical models are essential for early medical diagnostics, *in silico* planning of surgery, therapy and rehabilitation procedures. Traditional contour and spectral analyses of the waveforms as well as novel wave-intensity analysis, fractal analysis and other mathematical methods revealed important information on the state of arteries, vessel wall, microcirculation, general and specific diseases and pathologies. The most part of numerical computations of the blood flow in human systemic arteries have been carried out on the 55-tube model that had been developed on cadaveric dissections [2]. The lengths L_j and diameters d_j of the largest arteries of human trunk, head, upper and low extremities have been measured in the state of their maximal vasodilatation. In this study blood flow and wave propagation along aorta are studied on the 84-tube model of aorta (Fig.1a) based on the cadaveric and *in vivo* ultrasound measurements when the arteries are in their natural state [3].

Aorta is the largest blood vessel that directs the blood flow [4] and distributes it between the organs, muscles and other tissues via its branches. Due to its high elasticity the aorta converts the pulsatile flow produced by heart to almost steady flow in peripheral vessels (the Windkessel effect) [1]. Periodic heart contractions generate small excitations of blood pressure and velocity which propagate as PWs along the aorta with the pulse wave velocity (PWV) $c = 5-10$ m/s which significantly exceed the average blood flow velocity $u = 0.5-0.8$ m/s [1]. The propagating PWs experience numerous reflections at arterial



branching, narrowing (stenosis), enhancements (aneurysms), regions with low or high wall compliance (atherosclerotic plaques or age-related wall degeneration). Therefore, PW propagation and reflection in the aorta are of great interest [5]. Wave reflections influence the proximal aortic pressure and play a role in systolic hypertension [6]. Significant wave reflections originate due to narrowing between the thoracic and abdominal aorta [7].

PWV value is an important index of the arterial stiffness which well correlates with a risk of cardiovascular disease and has been shown to be an independent predictor of cardiovascular outcome [8]. Aortic, brachial and femoral PWVs determine probability of cardiovascular survival of patients with kidney failure [9] and patients with Marfan syndrome [10], ageing and hypertension [11]. 3D CFD modeling was found useful for detection of rigid inclusions in the aortic wall by the PWV values [12].

In this paper the most detailed model of human aorta as a tapered tube composed from 34 segments with 57 branches is developed and validated by the *in vivo* ultrasound measurements of the blood pressure $p(t)$ and flow $u(t)$ signals, and compared to the numerical data obtained in literature on different simplified geometries.

2. Mathematical modeling of the pulse waves in arteries

According to the theory of pulse waves in arteries as fluid filled compliant tubes developed by Sir. J. Lighthill [13], the wave propagation and reflection at the arterial branching are determined by local properties of the parent and daughter arteries, i.e. their characteristic wave admittances

$$Y_0 = \frac{\pi d^2}{\rho_b c_0}, \quad c_0 = \sqrt{\frac{Eh}{\rho_b d}}, \quad (1)$$

where c_0 is the pulse wave speed by the Moens-Korteweg formula, ρ_b is the density of blood, d, E, h are diameter, Young modulus and wall thickness of the artery.

In that way, the wave reflection coefficient $\Gamma = p_r / p_i$ which is the ratio of the amplitudes p_r and p_i of the reflected and incident waves is determined as [13]

$$\Gamma = \frac{Y_0^{(0)} - \sum_{j=1}^m Y_0^{(j)}}{Y_0^{(0)} + \sum_{j=1}^m Y_0^{(j)}}, \quad (2)$$

where the superscript indicates the number of the artery in the branching; (0) is for the parent artery, $j=1, 2, \dots, m$ are for the daughter arteries; $m=2$ for the bifurcations, $m=3$ for the trifurcations, etc.

Accounting for the blood and arterial wall viscosities, the Womersley model [1] of the axisymmetric pulsatile flow of a viscous fluid along the viscoelastic tube can be used for generalization of the pulse wave theory. Then the wave speed instead of (1) is a complex value

$$c = c_r + Ic_i = c_0 \sqrt{\frac{1 - F_{01}}{1 - \sigma^2}} e^{i\theta}, \quad (3)$$

where c_0 is determined by (1), $F_{01} = 2J_1(\beta)/(\beta J_0(\beta))$ is the Womersley function, J_0, J_1 are the Bessel functions of the first kind and orders 0 and 1, accordingly, $\beta = \alpha(I)^{3/2}$, $I = \sqrt{-1}$, $\alpha = d\sqrt{\omega\rho_b/4\mu}$ is the Womersley number, ω is the wave angular frequency, σ is the Poisson ratio of the wall material, θ is the phase shift between the pressure and the wall displacement due to the wall viscosity [14].

The pressures $P^{(j)}(t, x_j)$ and volumetric flow rates $Q^{(j)}(t, x_j)$ in the j -th artery can be computed as superpositions of the incident and reflected running waves in the form [1]

$$\begin{aligned} P^{(j)}(t, x_j) &= P_0^{(j)}(e^{I\omega(t-x_j/c_j)} + \Gamma_j e^{I\omega(t+(x_j-2L_j)/c_j)}), \\ Q^{(j)}(t, x_j) &= Y_0^{(j)} P_0^{(j)}(e^{I\omega(t-x_j/c_j)} - \Gamma_j e^{I\omega(t+(x_j-2L_j)/c_j)}), \end{aligned} \quad (4)$$

where j is the number of the vessel, $P_i^0 = P_i|_{x_i=0}$ is the wave amplitude at the inlet of the artery, $x_j \in [0, L_j]$ is the longitudinal coordinate computed from the inlet, L_j is the length of the artery.

According to (6), any positive wave reflection ($\Gamma > 0$) leads to an increase in the pressure amplitude and decrease in the flow rate because any reflected wave carries some fluid against the flow. When the downstream wave admittance is bigger than the upstream one and $\Gamma < 0$, the so called negative wave reflection is observed. Then the reflected wave propagates downstream and brings additional amount of fluid that leads to the decrease in the pressure at the outlet and, therefore, in the increase of the flow rate by the increased pressure drop along the artery (suction effect). Negative wave reflections have been found in the pulmonary circulation [15], coronary vasculature [16,17], and some others [3,18].

3. Materials and methods

The values of $\{L_j, d_j\}_{j=1}^{91}$ of the aortic segments and its branches (Fig.1) have been measured on five cadavers during the post-mortem examination. The $p(t)$ and $v(t)$ patterns in different locations along the aorta (marked in Fig.1 by capital letters A-G) have been measured on five healthy volunteers (ages from 18 to 42) by triplex scanner 'Sonoline Elegra Advanced' (Siemens). The $p(t)$ and $v(t)$ curves in the main coronary arteries have been measured by transesophageal ultrasound. The measured curves have been smoothed by Bayesian filter (Fig.2) and analyzed. In total 150 pairs of $v(t)$ and $p(t)$ curves have been recorded and treated (30 measurement sites per an individual). The measurement data are presented in Table 1. The Roman numeration corresponds to the direction from the aortic root to bifurcation. The averaged non-scaled data (model I) and scaled to $h=175$ cm, and inlet diameter $d=35$ mm (model II) are marked by $\langle L \rangle, \langle d \rangle$.

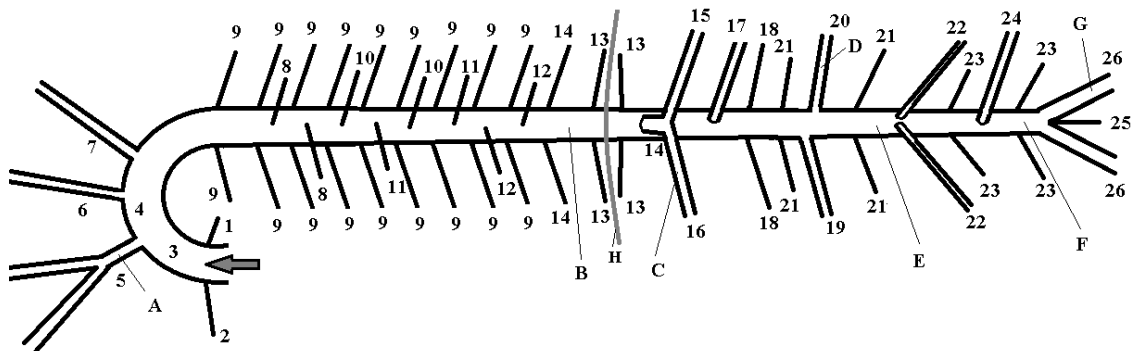


Figure 1. Model of aorta: left (1) and right (2) coronary, aortic root (3) and arc (4), brachiocephalic trunk (5), left carotid (6), subclavian (7), bronchial (8), intercostal (9), esophageal (10), mediastinal (11), pericardial (12), diaphragmal (13), subcostal (14), cervical trunk (14), splenic (15), hepatic (16), upper mesenchymal (17), suprarenal (18), left (19) and right (20) renal, upper lumbar (21), testicular (22), lower lumbar (23), lower mesenchymal (24), sacral (25) and iliac (26) arteries; the arrow indicates blood inflow; letters A-G correspond to the sites of *in vivo* measurements, H - diaphragm

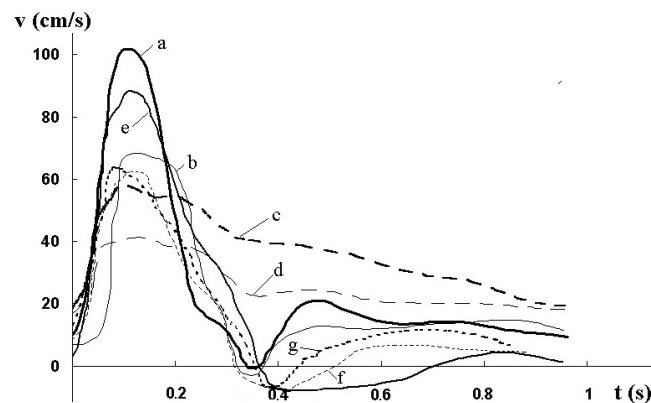


Figure 2. Digitized flow velocity curves $v(t)$; letters A-G correspond to the locations marked in Fig.1

Table 1. Diameters (d) and lengths (L) of the arterial segments in five humans h1, h2, h3, h4, h5 (height/age), males (m) and females (f), model I and model II averaged values

N	name	h1(m) d(mm)	l72/60 L(mm)	h2(m) d(mm)	l77/58 L(mm)	h3(f) d(mm)	l64/38 L(mm)	h4(f) d(mm)	l55/43 L(mm)	h5(m) d(mm)	l72/62 L(mm)	<d> (model I)	<l> (model I)	<d> (model II)	<l> (model II)
1	ascending aorta I	33	3	33.3	3	32	3	29	3	35	3	32.5	3.0	35.0	3.1
2	ascending aorta II	33	91	26.7	85	32	58	29	60	35	85	31.1	75.8	33.6	78.5
3	aortic arch I	32	23	32	23	30	15	29	4	35	6	31.6	14.2	34.1	14.6
4	aortic arch II	32	14	32	14	30	14.5	29	5	35	17	31.6	12.9	34.1	13.3
5	thoracic aorta I	31	1	23.5	5	30	2	29	6	29	24	28.5	7.6	30.9	7.9
6	thoracic aorta II	31	2	23	51	30	4	29	7	29	8.5	28.4	14.5	30.8	14.7
7	thoracic aorta III	31	2.5	23	2	30	3	29	2	29	1.5	28.4	2.2	30.8	2.3
8	thoracic aorta IV	31	21	22	22	30	23	29	12	29	9	28.2	17.4	30.6	18.1
9	thoracic aorta V	31	18.5	22	17	30	19	29	8	29	4	28.2	13.3	30.6	13.8
10	thoracic aorta VI	30.5	32	21.5	10	30	10	28	12	29	25	27.8	17.8	30.1	18.4
11	thoracic aorta VII	30.5	15	21.5	5	29.5	8	28	10	29	13	27.7	10.2	30.0	10.7
12	thoracic aorta VIII	30.5	17	21.5	15	29	18	28	22	29	12	27.6	16.8	29.9	17.7
13	thoracic aorta IX	30.5	32	21.5	15	29	18	28	22	29	25	27.6	22.4	29.9	23.4
14	thoracic aorta X	30	20	21.5	11	27	18	28	14	29	25	27.1	17.6	29.3	18.3
15	thoracic aorta XI	30	12	21.5	4	27	11	28	8	29	11	27.1	9.2	29.3	9.6
16	thoracic aorta XII	30	32	21	15	27	7	28	22	29	14	27.0	18.0	29.2	18.8
17	thoracic aorta XIII	29	32	21	15	25	18	28	22	29	25	26.4	22.4	28.6	23.4
18	thoracic aorta XIV	29	16	21	10	25	9	28	22	29	25	26.4	16.4	28.6	17.2
19	thoracic aorta XV	28.5	16	21	5	24	9.5	28	10	29	12	26.1	10.5	28.3	11.0
20	thoracic aorta XVI	28	32	21	15	23	17.5	28	12	29	13	25.8	17.9	27.9	18.6
21	thoracic aorta XVII	28	32	20.5	15	23	18	28	22	29	25	25.7	22.4	27.8	23.4
22	thoracic aorta XVIII	26	18	19.5	17	20	6.5	23	4	26	14.7	22.9	12.0	24.7	12.3
23	thoracic aorta XIX	25.7	20	19	18	20	8.5	23	4	26	27	22.7	15.5	24.6	15.8
24	abdominal aorta I	24	9	18	8	20	6	22	11	26	13	22.0	9.4	23.8	9.8
25	abdominal aorta II	23.6	33	17	44.5	19.5	12	22	13	25	34	21.4	27.3	23.2	27.9
26	abdominal aorta III	23	1	19	8.5	19	10	20	4	24	6	21.0	5.9	22.7	6.1
27	abdominal aorta IV	23	1	19	9.5	19	11	22	8	24	5	21.4	6.9	23.1	7.3
28	abdominal aorta V	23	1	20	14	19	12	20.5	12	24	17	21.3	11.2	23.0	11.7
29	abdominal aorta VI	22.5	19	20.5	12.5	19	10	20.5	7.5	23.5	14	21.2	12.6	22.9	13.0
30	abdominal aorta VII	22.5	2	20.5	2.5	19	2	20	1.5	23	3	21.0	2.2	22.7	2.3
31	abdominal aorta VIII	22.5	8	21	6	18.5	10	20	7	23	14	21.0	9.0	22.7	9.4
32	abdominal aorta IX	22	41	20	28	18	21	20	21	23	30	20.6	28.2	22.2	29.2
33	abdominal aorta X	22	18	20	8	18	13	20	18	23	16	20.6	14.6	22.2	15.3
34	abdominal aorta XI	22	23	19	22	17.5	11	19	12	21	16	19.7	16.8	21.3	17.3
35	abdominal aorta XII	22	24	19	26	17	20	19	21	21	30	19.6	24.2	21.2	25.1

36	abdominal aorta XIII	22	23	20	24	17	19	19	17	21	28	19.8	22.2	21.4	23.0
37	right coronary	3.1	37	3.5	38	6.3	26	3	48	2.7	35	3.7	36.8	4.0	38.6
38	left coronary	3.9	29	4.9	29	6.5	24	3.8	11	2.9	15	4.4	21.6	4.8	22.3
39	brachiocephalic trunk	19	42	11	36	13.5	35	11	36	16	31	14.1	36.0	15.2	37.6
40	left common carotid	8.8	109	7.3	116	8.5	110	7.2	117	10.5	130	8.5	116.4	9.1	121.5
41	left subclavian	12	64	13.7	44	8	26	7	29	10.5	35	10.2	39.6	11.0	40.9
42	bronchial	1.8	36	1.4	35	1.2	30	1	23	1.3	28	1.3	30.4	1.4	31.5
43	esophageal	2.4	28	1.8	27	1.6	25	0.8	19	1.2	26	1.6	25.0	1.7	26.0
44	mediastinal	1.5	2	1.1	25	1.2	23	1.2	16	1.4	24	1.3	18.0	1.4	18.8
45	pericardial	1.2	21	1	25.5	1.2	20.5	1.1	15	1.2	22	1.1	20.8	1.2	21.6
46	intercostal I	3.2	23	2	22	2.9	12	2.5	9	2.5	14	2.6	16.0	2.8	16.5
47	intercostal II	3.1	23	2.5	22	2.9	11	2.3	9	2.2	15	2.6	16.0	2.8	16.5
48	intercostal III	3	23.5	2.7	22	2.9	10.5	2.3	8	2.2	15	2.6	15.8	2.8	16.2
49	intercostal IV	3	23	2.5	22.5	2.9	11	2.3	8	2.2	14	2.6	15.7	2.8	16.1
50	intercostal V	3	23	2.5	22	2.9	11.5	2.3	8	2.1	16	2.6	16.1	2.8	16.5
51	intercostal VI	3.1	22.5	2.4	22	2.9	10.5	2.2	8	2.2	15	2.6	15.6	2.8	16.0
52	intercostal VII	3	23	2.5	22	2.9	11	2.2	8	2.2	15	2.6	15.8	2.8	16.2
53	intercostal VIII	3	23	2.5	22	2.9	11	2.3	8	2.2	16	2.6	16.0	2.8	16.4
54	intercostal IX	3	23	2.4	21.5	2.9	15	2.3	7	2.1	16	2.5	13.8	2.8	14.1
55	subcostal	3	23	2.5	22	2.9	11	2.3	7	2.1	14	2.6	15.4	2.8	15.8
56	phrenica superior	2	131	1.8	19	2.1	10	1.4	32	1.5	176	1.8	73.6	1.9	75.6
57	phrenica inferior	2	131	1.8	18	2.2	9	1.5	36	1.6	155	1.8	69.8	2.0	71.8
58	celiac trunk	8.9	11	7.5	11	8	17	8.7	14	10	15	8.6	13.6	9.3	14.3
59	upper mesenteric	8	67	8.5	19	9.8	47	13	17	7	17	9.3	33.4	10.2	34.7
60	suprarenalis	1	28	1.5	22	1.1	19	1	23	1.4	26	1.2	23.6	1.3	24.6
61	lumbar I	2	46	1.8	158	3	56	1	23	2.2	38	2.0	64.2	2.1	65.5
62	left kidney	6	41	4.3	53	8.5	87	5.6	37	4.4	68	5.8	57.2	6.3	59.6
63	right kidney	5.4	28	4.2	69	8.5	45	6.7	47	4.1	54	5.8	48.6	6.3	50.5
64	gonadal	1.5	310	1.3	340	1.8	300	1	223	2	250	1.5	284.6	1.6	295.6
65	lumbar II	2	46	1.7	158	3	56	2.6	50	2.2	38	2.3	69.6	2.5	71.6
66	lumbar III	2	46	1.7	158	3	56	2.6	50	2.2	38	2.3	69.6	2.5	71.6
67	lower mesenteric	5.5	50	3.5	26	3.5	28.5	3	43	4	52	3.9	39.9	4.2	41.7
68	lumbar IV	2	46	1.7	158	3	56	2.6	50	2.2	38	2.3	69.6	2.5	71.6
69	left iliac	13.5	69	11	38	10	52	10	70	10	57	10.9	57.2	11.8	60.1
70	lumbar V	2	46	2.1	158	3	56	2.6	50	2.2	38	2.4	69.6	2.6	71.6
71	right iliac	13.3	67.5	11	53	10	52	8.3	53	12	53	10.9	55.7	11.7	58.1
72	sacral	0.7	87	1.4	97	1.4	70	1.4	67	1.5	75	1.3	79.2	1.4	82.2

4. FSI mathematical model

Here 2D fluid-structure interaction axisymmetric model [1] of the pulsatile blood flow along a thick wall viscoelastic tube has been used for detailed computer simulations. The model is based on axisymmetric incompressible Navier-Stokes equations for blood flow

$$\nabla \cdot \vec{v} = 0, \quad \rho_f \left(\frac{\partial \vec{v}}{\partial t} + \vec{v} \cdot \nabla \vec{v} \right) = -\nabla p + \mu_f \Delta \vec{v}, \quad (5)$$

where \vec{v} is the flow velocity, ρ_f, μ_f are the fluid mass density and viscosity, p is the hydrostatic pressure, and the mass and momentum balance equations for the incompressible wall

$$\nabla \cdot \vec{u} = 0, \quad \rho_w \frac{\partial^2 \vec{u}}{\partial t^2} = -\nabla p_w + \nabla \cdot \hat{\sigma}, \quad (6)$$

where \vec{u} , ρ_w , p_w , $\hat{\sigma}$ are the displacement, density, hydrostatic pressure and stress tensor of the wall.

The Kelvin-Voigt rheological model is taken for the viscoelastic arterial wall

$$\tau_w \frac{\partial \sigma_i}{\partial t} + \sigma_i = A_{ik} \varepsilon_k + \mu_w \frac{\partial \varepsilon_i}{\partial t} \quad (7)$$

where A_{ik} is the matrix of the elasticity coefficients, μ_w is the wall viscosity, τ_w is the stress relaxation time, $\vec{\sigma}$ and $\vec{\varepsilon}$ are the stress and strain vectors in the form $\vec{a} = \{a_{11}, a_{22}, a_{33}, a_{23}, a_{13}, a_{12}\}$.

The continuity conditions for pressures and velocities at the fluid–solid interface in each vessel

$$r = 0: \quad \mathbf{v}_r = 0, \quad (8)$$

$$r = R: \quad \frac{\partial \bar{u}}{\partial t} = \vec{v}, \quad -p + \mu \frac{\partial v_r}{\partial r} = -p_w + \sigma_{rr}, \quad \mu \left(\frac{\partial v_x}{\partial r} + \frac{\partial v_r}{\partial x} \right) = \sigma_{rx}, \quad (9)$$

the attachment condition of the outer surface of the wall to the surrounding rigid tissues

$$r = R + h: \quad \bar{u} = 0, \quad (10)$$

have been taken as the boundary conditions for (5)-(7).

The inlet pressure wave into the aortic root has been taken from the in vivo measurement data [1] as a Fourier expansion with 6 harmonics

$$x = 0: \quad p^{(1)}(t) = \sum_{k=0}^6 P_k^{(1)} e^{i\omega_k t} \quad (11)$$

where $P_k^{(1)}$ are amplitudes of the harmonics with angular velocities ω_k .

The arterial wall is considered as composed of an incompressible isotropic material with radius dependent Young modules $E^{(j)}(R_j)$ [1]. The approximations for $E^{(j)}(R_j)$ and for the term $E^{(j)}(R_j)h^{(j)}(R_j)$ needed for the PWV calculations on (1) have been taken from [19], though in some models of aorta the constant Young modulus $E = 225$ kPa has been used [20]. In the 55-tube model [2] higher wall rigidity have been used: $E = 0.4$ MPa for aortic wall, $E = 0.8$ MPa and $E = 1.6$ MPa for its larger and smaller branches accordingly. The approximation for c_0 was accepted from the approximation $(Eh/\rho_b d) = 15.18 \cdot d^{-1.0514}$ with the coefficient of determination $R^2 = 0.8296$ [2]. The approximation for the aortic wall thickness has been taken from [20] in the form

$$h(d) = R_0(0.2802 \cdot \exp(-5.053R_0) + 0.1324 \exp(-0.1114R_0)),$$

where the local unperturbed radius $R_0(x)$ in every arterial segment is determined from linear interpolation between the inlet R_{in} and outlet R_{out} radii: $R_0(x) = R_{in} - (R_{in} - R_{out})x/L$.

Solution of (5)-(7) has been found in the form of the running waves

$$f(t, r, x) = \sum_{j=0}^{\infty} f_j(r) e^{i\omega_j(t-x/c_j)} \quad \text{for } f = \{v_x, v_r, u_x, u_r, p, p_w\}. \quad (12)$$

The numerical procedure for the FSI problem is described in detail and validated in [21]. The following material parameters have been used for numerical simulations: $\rho_b = 1.05 \text{ kg/m}^3$, $\mu_b = 4 \cdot 10^{-3} \text{ Pa} \cdot \text{s}$, $\rho_w = 1.12 \text{ kg/m}^3$, $\tau = 0.045 \text{ s}$, $\tau_2 = 0.035 \text{ s}$, $\sigma = 0.5$. The wall thickness and elasticity have been approximated as it is explained before. The structured tree data $Y_{ij}^{(k)}(\omega_j, \phi_j(d^{(k)}), \psi_j(d^{(k)}))$ have been taken from [20].

5. Results and discussions

The pressure and flow waveforms have been computed in the middle cross section of each segment in the aortic model (Fig.1) and the correspondent dependencies measured *in vivo* at different locations have been used for validation. The digitized signals (Fig.2) has been presented as Fourier series and compared to the correspondent harmonics of the computed signals in the form (12). The first harmonics in the solution (12) has been determined by the individual heart beat rate taken from the ultrasound data.

It was found, small variations in the parameters ϕ_j, ψ_j that determine the terminal structured outflow trees influenced the pressure and flow oscillations in the closest tube only, while the signals in other tubes remain almost the same, with minor differences. It may be connected to fast attenuation of the reflected waves and small input of the multiple reflections. In that way, when the measured inlet pressure profile has been used in the form (16), the first computations of the pressure and flow signals in the sites A-G exhibited noticeable differences with the measured signals when the initial $\phi_j = 1, \psi_j = 1$ values has been used (Fig.4). When the calibration procedure for ϕ_j, ψ_j values has been conducted by the least square method, the computed curves became quite close to the measured signals (Fig.3). In that way the structured tree outflow boundary conditions at the terminuses provide better approximation giving different wave impedances for different harmonics [19]. In the 1D model the terminal admittances are also determined by two parameters of the Windkessel model, e.g. frequency independent resistivity and capacity [1]. Despite the 1D model, the model (5)-(11) describes wave dispersion and wave propagation in the fluid and viscoelastic walls.

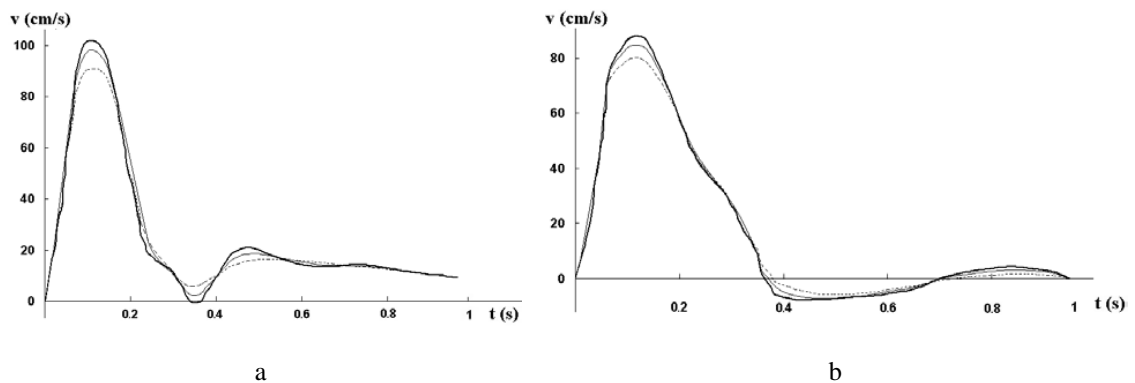


Figure 3. Blood flow velocity measured (thick solid) and computed before (dashed line) and after (thin solid line) the corrections, at the locations A (a) and E (b) (see Fig.1)

After validation, the averaged values $\langle \phi_j \rangle, \langle \psi_j \rangle$ have been computed for the averaged geometrical models I (Fig.4) and II (Fig.5) dimensions (Table 1). An example of numerical computations on the averaged model is presented in Fig.4. The main features of the pulse wave propagation along aorta i.e. increase in the pressure amplitude and steepening, appearance of the dicrotic wave due to wave reflections, decrease of the flow amplitude and absence of the reverse flow at the end systole, are presented in the computed curves. The same signals computed for the model II scaled to the height $h=175$ cm give more smooth curves for the same input data. This may be connected with big differences in the lengths of the aortic segments of the taller individuals ($h=172, 177$ cm) and shorter ones ($h=155, 164$ cm).

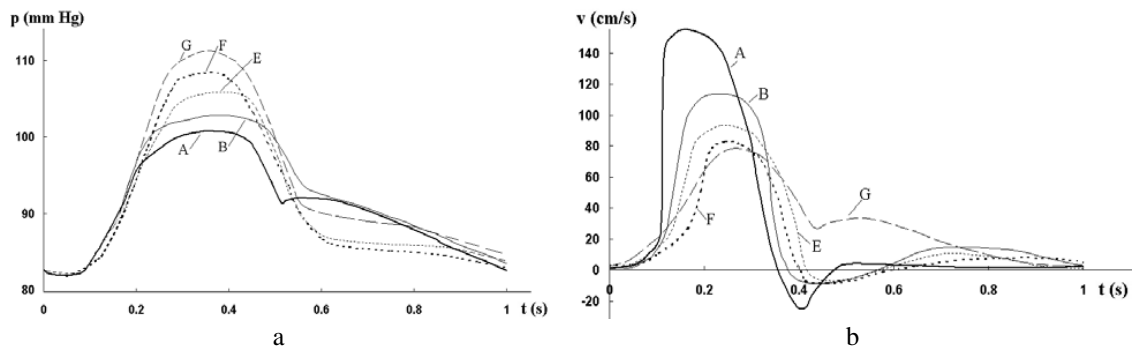


Figure 4. Blood pressure (a) and flow (b) waveforms in the locations A,B,E,F,G of the averaged model

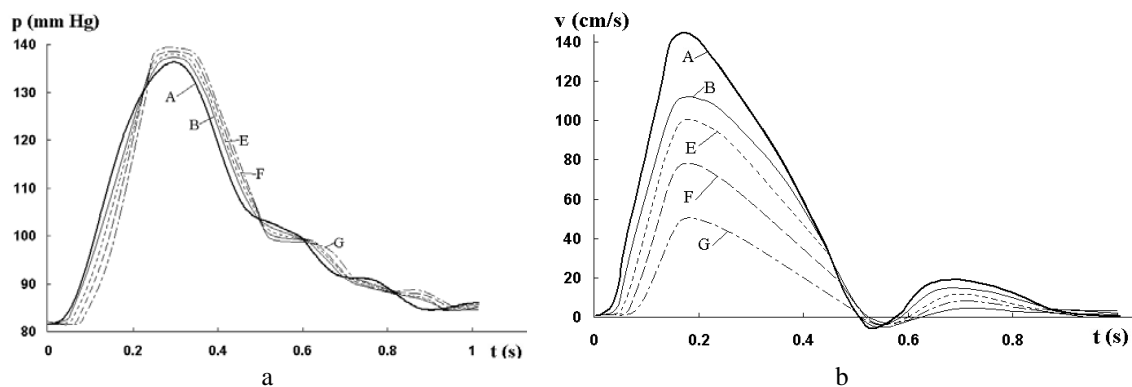


Figure 5. Blood pressure (a) and flow (b) waveforms in the locations A,B,E,F,G of the scaled models

The data on the arterial diameters are more uniform than on the lengths that produce significant differences in the phases of the waves reflected at the same branches in different individuals. For instance, the aortic length between the inlet and aortic bifurcations varied between 58-72cm. When the individual dimensions are scaled by the personal height, and then averaged and scaled to a fixed height, it produces fewer differences between personal specific coordinates of the same branches along the aorta.

6. Summary

Based on personal MRI of CT-extracted individual geometry of the larger blood vessels, the corresponding 3D structure can be restored and the hemodynamic parameters $p(t)$, $v(t)$, PWV and WSS can be computed. The smallest vessels remain invisible and the proper boundary conditions are needed for the CFD simulations. Here the most detailed aortic model composed from 34 straight segments with 57 side branches is developed on the measurement data. It was shown, the average geometrical model rescaled by individual height of the individual exhibit steady flow and wave propagation properties similar to those known from literature. Most of the side branches promote wave reflections along the flow, not upstream, that produces lower pressure at the outlets of the aortic segments and flow acceleration due to the suction effect.

The presented mathematical model gives more realistic results than those obtained on 3d geometries with rigid walls. The test computations revealed physically consistent pressure wave peaking and steepening along aorta, and blood flow decrease in the amplitude, negative flow phase at the end systole and dicrotic wave appearance and development due to the wave reflections. The major input in the dicrotic wave is produced by aortic bifurcation [1].

The developed mathematical model allows fast numerical computations for different geometries. The scaled model II can be 'adjusted' for any individual when the inlet and outlet diameters of the aorta and height are measured. The boundary conditions can be reconstructed from $p(t)$ and $v(t)$ curves measured on 6-10 arteries by US. The model can predict high reflection sites that are dangerous for wall damage. It can be also useful for modeling the hydrodynamic outcomes of aortic stenosis, aneurism and other pathologies, as well as early diagnoses of them.

The authors are grateful to organizers and participants of the XXIII Fluid Mechanics Conference KKMP2018 (Zawiercie, Poland, 9 -12 September 2018).

References

- [1] Nichols W and O'Rourke M 2005 *McDonald's, blood flow in arteries. Theoretical, experimental and clinical principles* (Oxford: Oxford Univ. Press)
- [2] Westerhof N, Bosman F, de Vries C J and Noordegraaf A 1969 *J. Biomech* **2** pp 121-143
- [3] Kizilova N, Philippova H and Zenin O 2010 *Mechanika w Medycynie* vol 10 ed Korzynski M and Cwanka J (Rzeszow: Rzeszow Univ. Press) pp 103-118
- [4] Daves J E, Parker K H, Francis D P, et al. 2008 *Heart* **94** pp 1545-1547
- [5] Nguyen K T, Clark Ch D, Chancellor Th J and Papavassiliou D V 2008 *J. Biomech.* **41** p 11-19
- [6] Westerhof B E, Guelen I, Westerhof N, et al. 2006 *Hypertension* **48** pp 595-601
- [7] Latham R D, Westerhof N, Sipkema P, et al. 1985 *Circulation* **72** pp 1257-1269
- [8] Vappou J, Luo J, Okajima K, et al. 2011 *Artery Res.* **5** pp 65-71
- [9] London G M and Pannier B 2010 *Nephrol. Dial Transplant.* **25** pp 3815-3823
- [10] van der Palen R L F, Barker A J, Bollache E, et al. 2017 *J. Cardiovasc. Magn. Resonance* **19** 10.1186/s12968-017-0345-7
- [11] London G M and Guerin A P 1999 *Am. Heart J.* **138** pp 220-224
- [12] Shahmirzadi D and Konofagou E E 2012 *Artery Res.* **6** pp 114-123
- [13] Lighthill M J 1978 *Waves in fluids* (Cambridge: Cambridge Univ. Press)
- [14] Bergel D H 1961 *J. Physiol.* **156** pp 458-469
- [15] Hollander E H, Wang J J, Dobson G M, et al. 2001 *Am. J. Physiol.* **281** pp 895-902
- [16] Sun Y-H, Anderson T J, Parker K H and Tyberg J V 2000 *J. Appl. Physiol.* **89** pp 1636-1644
- [17] Zenin O K, Kizilova N N, Philippova E N 2007 *Biophysics* **52** pp 924-930
- [18] Kizilova N N 2007 *Biophysics* **52** pp 131-136
- [19] Olufsen M S 1999 *Am. J. Physiol.* **276** pp 257-268
- [20] Blanco P J, Watanabe S M, Passos M A, et al. 2015 *IEEE Trans. Biomed. Eng.* **62** pp 736-753
- [21] Hamadiche M and Kizilova N N 2005 *Intern. J. Dynam. Fluids* **1** pp 1-23